Acta Materialia 188 (2020) 570–578

Contents lists available at ScienceDirect

Acta Materialia

journal homepage: www.elsevier.com/locate/actamat

Full length article

Deformation mechanism maps for sub-micron sized aluminum

De-Gang Xie[a], Rong-Rong Zhang[a], Zhi-Yu Nie[a], Jing Li[a], Evan Ma[c], Ju Li[b,*], Zhi-Wei Shan[a,*]

[a] Center for Advancing Materials Performance from the Nanoscale (CAMP-Nano) & Hysitron Applied Research Center in China (HARCC), State Key Laboratory for Mechanical Behavior of Materials, Xi'an Jiaotong University, Xi'an 710049, China
[b] Department of Nuclear Science and Engineering and Department of Materials Science and Engineering, Massachusetts Institute of Technology, Cambridge, MA 02139, USA
[c] Department of Materials Science and Engineering, Johns Hopkins University, Baltimore, MD 21218, USA

ARTICLE INFO

Article History:
Received 29 August 2019
Revised 7 January 2020
Accepted 7 February 2020
Available online 13 February 2020

Keywords:
High temperature
Nanomechanics
In situ TEM
Size effect
Strength

ABSTRACT

Plastic deformation of sub-μm sized metals at different temperatures is influenced by factors absent in their bulk counterparts, including surface diffusion assisted softening and mechanical/thermal annealing-induced hardening. The test temperature and sample size therefore strongly affect the mechanical behavior, necessitating the construction of new deformation mechanism maps (DMM). Here, based on results from *in situ* quantitative compression tests on micro-pillars at various sizes and temperatures ranging up to 400°C, we have constructed DMMs for single-crystalline sub-micron-scale aluminum, consisting of elasticity, diffusive plasticity, and displacive plasticity regimes. In the sample size-stress DMM (for a fixed temperature), a "strongest size" is found at the triple junction of three regimes, above which "smaller is stronger", below which "smaller is weaker". In the diffusive plasticity regime, deformation is localized within the top pillar volume demarcated by a moving front interface, which is likely a newly formed grain boundary, that is impenetrable to impinging dislocations below a critical stress of ~1 GPa.

1. Introduction

At room temperature, many micro- and nano-scale metallic crystals exhibit a trend of "smaller is stronger", with strength approaching ideal 'pristine' samples [1, 2], resulting from mechanical annealing [3, 4] or thermal annealing [5]. The plastic flow often becomes irregular, with an intermittent stress–strain curve consisting of strain bursts [6–8]. For example, submicron-scale metals can sometimes collapse in a single giant strain burst in compression [1, 5], which we term "stochastic" behavior. Therefore, how to tame the wild strain burst to achieve a smooth, controllable plastic flow [9] without compromising the high strength is a challenge in nanomechanical engineering. In recent years, diffusive deformation, distinct from displacive deformation, has been proved to be a good way to enhance the formability of crystals, but at room temperature only below a critical sample size usually less than ten nanometers [10–13]. By incorporating slip-activated surface creep, this critical size can be increased to tens of nanometers [14]. However, between the upper limit of this critical size (a few tens of nanometers) and the lower size limit (above a few microns) for conventional ductile bulk crystal, there is still a size regime with uncontrollable plastic flow, where the "mechanical controllability index [9]" is exceptionally low.

A solution to this dilemma would be deforming at elevated temperatures. For centuries, metalworkers have known that increasing temperature can greatly improve the formability (lowered strength and enhanced ductility). This is due to the involvement of diffusive processes such as dynamic recovery, recrystallization and various mechanisms of creep (dislocation power-law creep, Nabarro–Herring creep and Coble creep) [15, 16]. Heating may be a method for improving the ductility of materials at micro- and nano-scales. The deformation of small-scale materials is widely known to have dependences on factors absent in their bulk counterparts, such as mechanical/thermal annealing-induced hardening [17], destabilization of pinning points by attraction to free surfaces [4], and surface oxide effects [18, 19]. These new behaviors at the micro- and nano-scale make the construction of DMM quite challenging. Since Ashby's work in 1972, there have been deformation mechanism maps (DMM) [20] established to delineate the dominant deformation mechanism under different combinations of temperature, stress and grain size, which are then used to guide the optimization of processing parameters [12, 20–23]. However, these DMMs are bulk-materials-based, not applicable to small-scale materials with relatively large surface-to-volume ratio. For materials at these small scales, there is no DMM yet, despite urgent need in various applications [24, 25].

In the past, construction of DMMs was primarily based on available phenomenological constitutive equations [20] for bulk materials or atomistic simulations [21]. However, both approaches need to be experimentally validated for micro- and nano-scale crystals. Due to

* Corresponding authors.
E-mail addresses: liju@mit.edu (J. Li), zwshan@mail.xjtu.edu.cn (Z.-W. Shan).

https://doi.org/10.1016/j.actamat.2020.02.013
1359-6454/

the temperature-sensitivity of dislocation behavior including nucleation [2, 26], migration [27–29] and interaction [30], prediction of the high temperature behavior of micro- and nano-scale crystals is challenging. Here we take the experimental route for constructing DMMs for submicron material samples. The best experimental choice is *in situ* quantitative nanomechanical testing inside TEM, since identification of dominant deformation mode can be more straightforward than other ex-situ methods, benefiting from the simultaneous acquisition of stress–strain data and real-time recording of microstructure/morphology evolution. In the past decades, *in situ* nanomechanical experiments were mostly carried out at room temperature [31, 32]. In this work, the conventional metallic sample mount was replaced by a quartz sample mount embedded with heating and sensing wires, as shown in Fig. 1. By attaching a metal foil onto the mount, multiple submicron pillar samples can be fabricated and tested efficiently in a single experimental session. To exclude the influence of different configurations of preexisting dislocations, all samples were thermally pre-annealed to a pristine dislocation-free state before the tests. Using this method, we systematically performed quantitative compression tests on submicron aluminum pillars with sizes ranging from ~100 nm to ~1 μm, under temperatures ranging from room temperature to 400 °C (0.72T_m for Al).

2. Experimental methods

Single crystal aluminum (99.9995%) disks were cut into 1.5 mm × 2 mm rectangular plates, which were mechanically polished to 100 μm in thickness and electrochemically thinned to a few microns at one edge. Submicron-sized cylindrical pillars were prepared by focus ion beam (FIB, FEI Helios NanoLab 600, operating at 30 keV) milling on the thinned edge. The milling current used in the last step was as low as ~20 pA to minimize geometrical taper and irradiation damage by ion beam. The thickness of surface affected layer was about 5 nm according to the TEM observation. All pillars had a taper angle of 2°–4° and an aspect ratio (top diameter/length) of 1/2–1/3.5.

The *in situ* TEM heating and nanocompression tests were performed by using a heater mounted onto a Hysitron PI95 PicoIndenter holder in an environmental TEM (Hitachi H9500, operating at 300 kV and 0.5–4 μA emission current). The crystal orientation of the pillar axis is ⟨110⟩ and the electron-beam direction is ⟨001⟩ for all the tested pillars. The heating and nanocompression tests were carried out in vacuum $<10^{-4}$ Pa. Before the nanocompression tests, all pillars were heated to 400 °C to thermally anneal out the preexisting dislocations and FIB damage, and then cooled down to the test temperature. The Hysitron PI95 holder comes with a diamond punch connected to a MEMS transducer, which has force resolution of ~300 nN and displacement resolution of ~2 nm. We used displacement control to apply constant loading rates, which were usually 7.5 nm/s for pillars of $D \geq 700$ nm, 5 nm/s for pillars of 700 nm$>D \geq$ 200 nm, and 3 nm/s for pillars of $D<200$ nm. The corresponding strain rates for all pillars are from 2.4–10.1 × 10^{-3} s^{-1}, roughly on the same order of magnitude. A commercially-available COMSOL software was used to estimate the real temperature of the pillar.

The drift rates of the punch and substrate were firstly measured from the video using Matlab and then used to corroborate with the original displacement data. By analyzing the video frame by frame, the displacement values of the tip and the substrate were dynamically tracked during compression test. The effectiveness of the tracking is reflected by the tight adherence of the tracking markers (short white horizontal lines) to their targets (the tip/substrate). Also, the tracking results are displayed as displacement values including the original displacement, the real displacement, the tip drift, and the pillar drift. Using these values, the real loading rate, the drift of the tip/substrate can be directly calculated. The tracking results show that the real strain rate deviates from the set value by less than 30%.

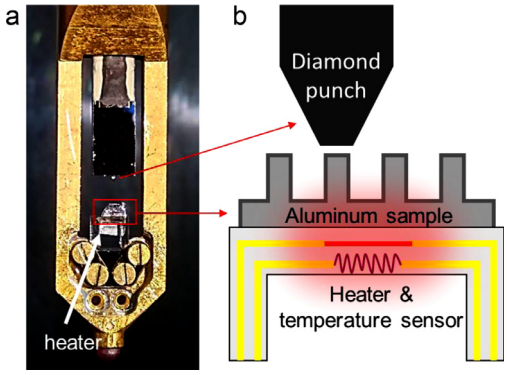

Fig. 1. Schematic of the experimental setup for high temperature *in situ* compression. (a) Picture of the front end of the TEM holder with a quartz sample mount, which comes with the heating and temperature sensing functions. (b) Schematic illustration of the compression experiment.

3. Results and discussion

3.1. Estimation of actual temperature in the pillars

Due to the cooling effect from the diamond punch, the pillar samples have a lower actual temperature than the set temperature, which shall be evaluated first. This actual temperature can be roughly estimated by using two kinds of observed data: the thermal expansion of the sample itself and the reading from the embedded sensor. Due to the thermal expansion, the edge of the aluminum foil, where the submicron pillars locate, would move forward by a distance of δ_0=~3.2 μm as temperature rose from 25 °C to 400 °C. But when a 400 °C pillar was compressed by a 25 °C punch, the backward displacement due to cooling was measured to be less than 20 nm (as shown by the pillar drift readings in Supplementary Movie s1-2), about 0.6% of δ_0. Since the thermal expansion of the aluminum is linearly related to the temperature change under our experimental condition, the average temperature drop of the aluminum foil should also be about ~0.6%, i.e. 2.5 °C. This estimate is corroborated by the temperature reading from resistance temperature detector, which was ~1 mm away from the pillar samples. After turning off the feedback control, a small depression can be found on the temperature-time curve, which shows a maximum temperature drop of about 1.2–1.5 °C during compression of D = 580 nm pillars at 400 °C (see Fig. 2). Considering that both the aluminum foil and diamond punch have high thermal conductivity (thermal conductivity κ=238 W m^{-1} K^{-1} for aluminum and 990 W m^{-1} K^{-1} for diamond) and are well thermally isolated from the supporting structure (quartz mount with κ=1.46 W m^{-1} K^{-1} or 1-D silicon beams with equivalent diameters at micron-scale), the temperature

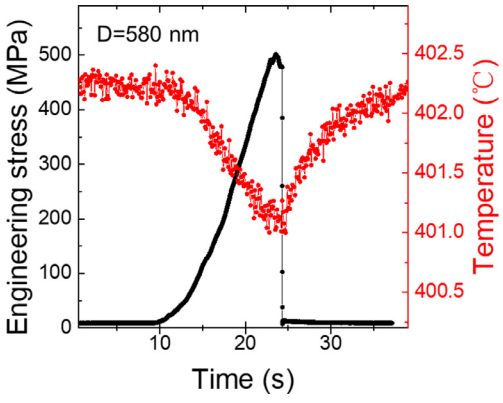

Fig. 2. Temperature change during compression of a pillar with diameter=580 nm.

distribution in both the tip and the aluminum foil can be expected to be nearly homogeneous.

The two experimental measurements above only represent the average temperature change in the aluminum foil, rather than the pillar itself. The best choice to exclude the effect of temperature gradient will be the repeating experiment with both the sample and the punch heated to the same temperature, but this approach is currently unavailable. Therefore, we choose finite element method (FEM) simulation to estimate the temperature distribution in the pillars. The geometry and the boundary condition of the model are depicted in Fig. 3a, in which a pillar sample with diameter of 400 nm and length of 1200 nm was created between the diamond punch and the aluminum substrate. On the surface of the pillar, a surface layer of 6 nm in thickness was created to mimic the aluminum oxide layer. The diamond punch and the aluminum were assigned thermal parameters of their bulk counterparts (Table 1), while the thin oxide layer was assigned a quite low thermal conductivity=0.4 $Wm^{-1} K^{-1}$ due to the size-induced quantum effect [33]. The top surface of the diamond punch was set at room temperature, while the bottom surface of the aluminum substrate was set at the heating temperature (100–400 °C).

The simulation result is shown in Fig. 3b and c. After thermal steady state was reached, the lowest temperature is found at the top part of the pillar. The temperature drops almost linearly with height from the top to the bottom. For all temperatures, the average temperature at the top will decrease by ~26%, while in the whole pillar by ~13%. It should be noted that based on this model, the cooling effect should be overestimated due to two reasons: (1) The boundary condition is simplified by directly setting the end plane of the diamond punch at room temperature, which will surely result in a stronger cooling effect. (2) The thermal resistance at the contact interface is neglected since we cannot find this parameter anywhere.

In summary, due to the cooling effect from the diamond punch, the real temperature change of the pillars is estimated to drop by less than 13% from the set temperatures. The following equation can estimate the real temperature

$$T_{real} = T_{set} - (T_{set} - 25^{\circ}C) \times 13\% \quad (1)$$

3.2. Electron beam effect

It has been reported that electron beam irradiation can promote the production of vacancies in aluminum, by kicking out atoms from the bottom surface of the foil sample [41]. Moreover, electron beam irradiation can result in temperature rise in the sample [42–44]. Theoretically, because diffusion in crystals is mainly mediated by vacancy exchange, the irradiated pillar with more vacancies usually exhibits enhanced diffusive plasticity [41, 45–47]. Therefore, to assess the real material property, electron beam effect on the deformation behavior at elevated temperature shall be determined.

For this purpose, two pillars with nearly the same diameter=~170 nm were compressed under the same temperature T_{set}=275 °C and strain rate, but one with beam-on, while the other

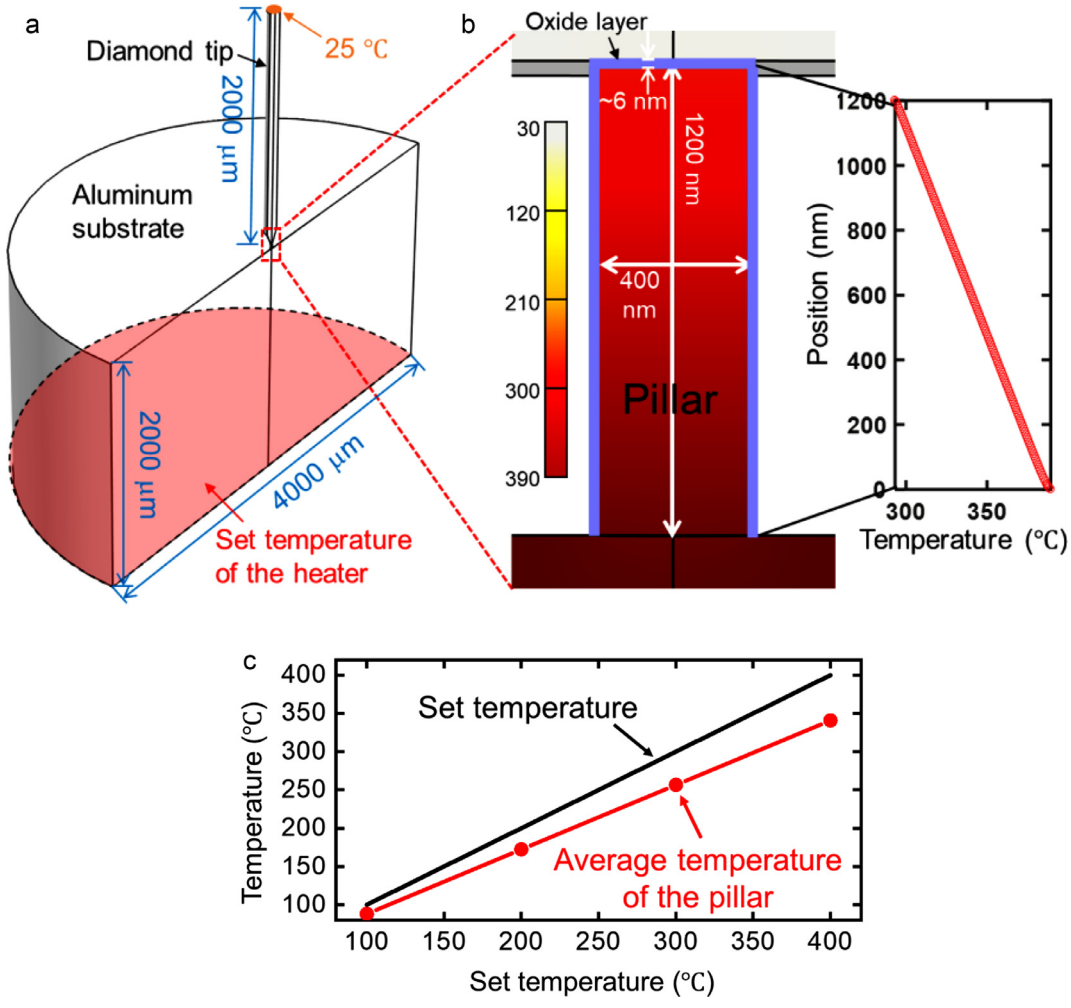

Fig. 3. Results of FEM modeling for estimating the actual temperature distribution in the pillar sample. (a) The constructed geometry and boundary conditions. (b) The temperature distribution in the pillar when the heater temperature is set at 400 °C. The insert plot at the right is the extracted temperature distribution along the central axis in the pillar. (c) Comparison of the average temperature with the set temperature at some typicalset temperatures.

Table 1
Thermal parameters used in the FEM simulation.

Materials	Heat capacity/ C_ρ [J/(kg · K)]	Thermal conductivity/ k [W/(m · K)]	Density/ρ [kg/m^3]
Aluminum	900	238	2700
Aluminum oxide	730	0.4 [33]	3965
Diamond (100)	520	990	3515

with beam-off. The engineering stress–strain curves were compared in Fig. 4. The two curves nearly overlapped, indicating that turning off the electron beam did not change the mechanical behavior substantially.

3.3. Mechanical behavior of annealed pillars

When the temperature is below a critical set temperature T_c=275 °C, the annealed submicron crystals exhibit a stochastic deformation behavior. Fig. 5 shows the typical result from a pillar sample with diameter of 359 nm and tested at 250 °C at strain rate of 3.7 × 10^{-3} s^{-1}. The stress–strain curve begins with a linear part of elastic deformation and then, a huge strain burst suddenly sets in, as shown in Fig. 5a. In the whole elasticity stage, the pillar remained pristine, without generating any dislocation storage even at the high stress of ~1 GPa, as evidenced by the clean bright field images extracted from the video at stress levels of ~800 MPa (Fig. 5c) and 1131 MPa (Fig. 5d), which is the last moment immediately before the burst. The strain burst boosts the strain from 3.7% up to a giant value of 44.7% (Fig. 5e), causing a few large slip steps at the surface. A previous study by Lee et al. [34] also reported compression results of annealed aluminum pillars at similar diameter D=~400 nm at room temperature. Unlike the single huge burst in our results, their results showed multiple discrete strain bursts with averaged strain jump of ~0.68% per burst. The yield/flow stress of the annealed sample is at the same level of <400 MPa as that of the as-FIBed sample, less than half of our experimental measurements. Another report with FIBed Cu pillars, also with face-centered-cubic crystal structure, showed that the flow behavior is largely unaffected after thermal annealing [35, 36]. The difference between their results and ours can be explained by the sample difference: The pillar samples in our work were well annealed to a lower dislocation density (0–2 dislocations, ρ_d=0–5 × 10^{12} m^{-2}, while in Lee's work, ρ_d >1 × 10^{13} m^{-2}) and had higher aspect ratio (>1/3.5, while Lee's work <1/4). Therefore, possible softening factors in our tests were eliminated due to two reasons: the first is that internal dislocation nucleation/multiplication are limited by lower preexisting dislocation density, and the other is that the bending/buckling during compression tests are more difficult in pillars with lower aspect ratio.

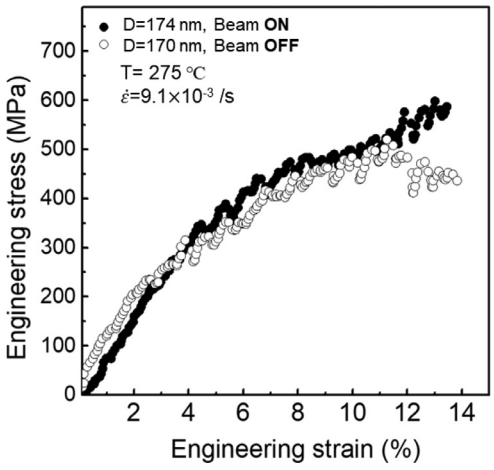

Fig. 4. Effect of electron beam on the mechanical behavior of sub-micron pillars at elevated temperatures.

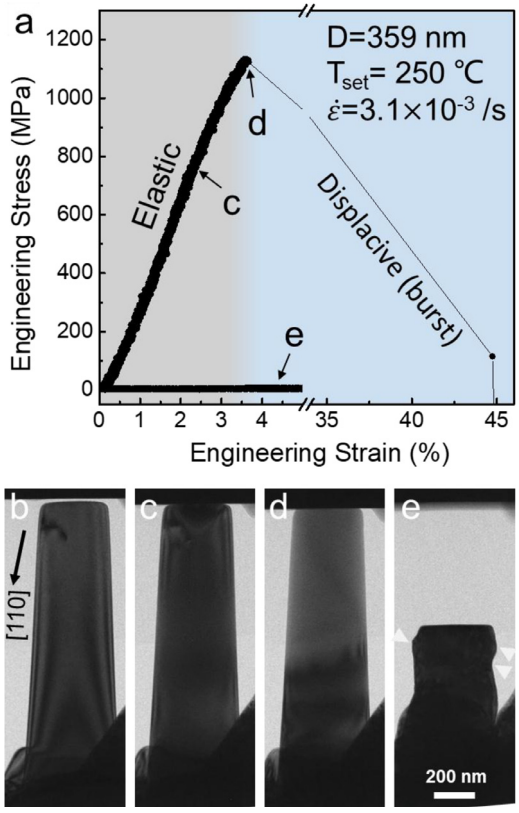

Fig. 5. A typical stochastic-type deformation process at relatively low set temperature and large size. (a) The stress–strain curve for compression tests performed with a pillar of diameter D = 359 nm at T_{set}=250 °C with a strain rate of 3.1 × 10^{-3} s^{-1} and loading direction near [110]. (b–e) Sequential images extracted from the video at moments indicated in (a). (b) and (e) are the pillar images before and after the compression tests, respectively. The white triangles indicate the surface steps resulting from the dislocation slip.

When the set temperature is above T_c=275 °C, the stress–strain curve clearly shows three distinctive stages, i.e. the elasticity stage, the diffusive-plasticity stage, and the displacive-plasticity stage. In Fig. 6 and supplementary movie s2, a pillar of diameter D = 373 nm is compressed at T_{set}=325 °C and strain rate of 4.2 × 10^{-3} s^{-1}. In the elastic stage under 750 MPa, the pillar remains pristine, as evidenced by the clear stress contours near the contact interface in Fig. 6c. Then, a transient stress drop of 70 MPa marks the beginning of the second stage, in which the stress–strain curve varies smoothly without obvious strain bursts or stress fluctuations until a critical stress σ_c=971 MPa is reached. At this critical stress, the third stage of displacive plasticity sets in with a giant strain burst from strain= 8% to strain=54%.

The complete deformation process of the second stage is shown in supplementary movie s2. At the beginning of this stage, the stress drop indicates the introduction of dislocation activity into the top of the pillar, reflected by the smeared image contrast immediately after the yield point. Then the top part of the pillar began to swell up and soon an interface developed, clearly dividing the deforming part from the undeformed part, as indicated with the dashed white line in Fig. 6d. After the interface is formed, localization of deformation intensified, as evidenced by the faster expansion of diameter than the downward advancement of the interface in supplementary movie s2. By digitally tracking the change of diameter of the deforming part, the true stress can be calculated and plotted in Fig. 6a versus the engineering strain, as indicated by the red dotted curve. While the

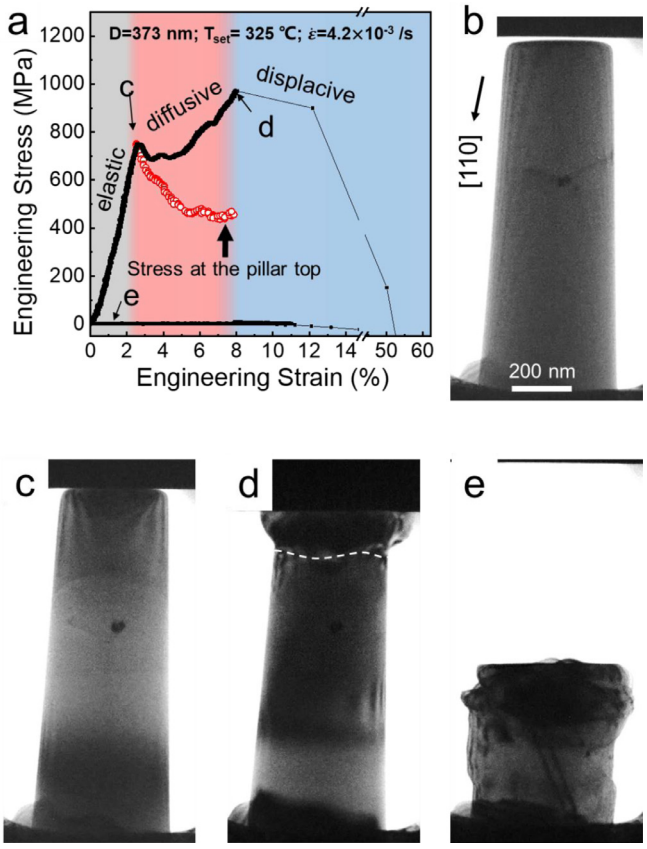

Fig. 6. A typical ductile-type deformation process for a pillar with diameter D = 373 nm at temperature T_{set}=325 °C and strain rate $\dot{\varepsilon}$=4.2 × $10^{-3}s^{-1}$. (a) The engineering stress–strain curve which shows three distinct periods. The red curve section represents the real stress at the top part of the pillar. (b) The bright field image of the well-annealed pillar before compression test. The compression is performed near [110] direction, as indicated with a black arrow. (c–e) The video snapshots showing the deformation process at moments indicated in (a). The internal interface between the plastically-deformed region and the elastically-deformed region is depicted with a white dashed line. (For interpretation of the references to color in this figure legend, the reader is referred to the web version of this article.)

original engineering stress–strain curve shows the "strain-hardening" phenomenon in the diffusive stage, the true stress–strain curve shows "strain softening". The mushroom shape formed after deformation is in strong contrast to the slip-band-dominated morphology after deformation at low temperatures, indicating that the deformation is no longer dislocation-slip-dominated. If the deformation strain is from purely shear-stress-driven dislocation glide, then it will produce shear offset along slip plane about 45° to the axis of the pillar, and the resulting deformation volume will extend far beyond the observed thin mushroom cap. Considering the continuous stress–strain curve and the mushroom-shaped small deformation volume with smooth surface, the second stage is believed to be dominated by diffusive plasticity, hence referred to as diffusive-plasticity stage.

The strain softening in true stress–strain curve (Fig. 6a) could arise due to dislocation pipe diffusion [30, 37]: the stored dislocation density increases with strain, providing more effective diffusion paths, which results in a stronger softening effect. The much smaller deformation volume can originate from short distance between nucleation site and climb or trapping site of dislocation, via a frustrated travel path originating from climb and cross-slip at elevated temperature. Although dislocation cross-slip and climb can be promoted by elevated temperature [38], the parameter space of temperature-stress combination for producing evident diffusive deformation has never been experimentally delineated before.

Despite vigorous evolution in the confined volume, the dislocations can hardly penetrate the aforementioned interface into the pristine part below. One plausible reason is that the interface is a highly dislocated interface, or even is a dislocation network, dynamically formed in a way similar to the formation of low angle boundary [39, 40]. It is quite challenging to characterize the dislocation structure at this interface, because in a deforming sample, this interface is at edge-on direction, while in a deformed sample, the dislocation structure will be annealed out. Despite those challenges of *in-situ* or post-mortem characterization, a glimpse of the dislocation structure can be occasionally captured in the video, as shown in Fig. 7a and b. At the interface, alternative bright/dark fringes can be seen, while below the interface, we see a clean interior without dislocation activity. This dislocated interface (likely a grain boundary) can catch and stop most incoming dislocations, as schematically illustrated in Fig. 7c. However, if the stress is high enough (> 1 GPa), dislocations can break through this interface, as well as emit from the corner under the mushroom-shaped cap. By this way the third stage, displacive plasticity, is initiated.

3.4. Construction of stress-temperature deformation mechanism map

Since historical DMM construction is related to the strain rate and grain size, equivalent to the pillar diameter in this work, we choose compression under different temperature intervals, on pillars within a narrow size and strain rate regime. With the consideration above, two groups of pillar samples with diameters of 350–418 nm were compressed at strain rate of 3.0–4.2 × $10^{-3}s^{-1}$ at set temperature between 25 °C and 400 °C. The first group of pillars was tested at temperature intervals of 100 °C, with two pillar samples for each set temperature to ensure reproducibility, and the engineering stress–strain curves are shown in Fig. 8a. At set temperatures of 100 °C, 200 °C, and 300 °C, the stress–strain curves are almost always composed of a segment of elasticity followed by a giant strain burst, and this kind of deformation will be referred to as stochastic-type. In contrast, at T_{set}=400 °C, both curves contain a continuous/serrated flow segment after the linear segment, referred to as ductile-type hereafter. The transition from the stochastic-type deformation to the

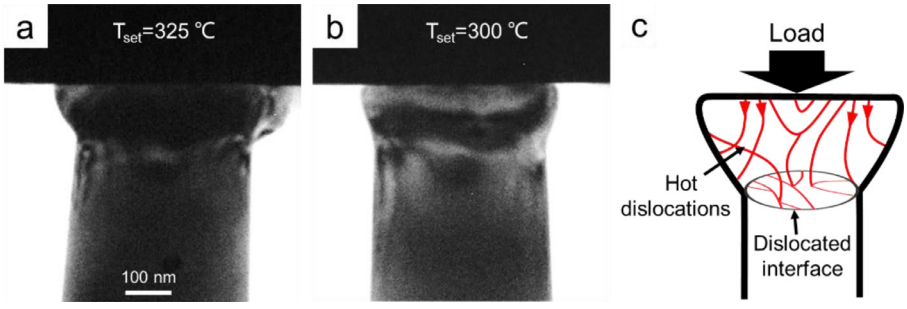

Fig. 7. The formation of a dislocated front interface between the plastically deformed volume and elastically deformed volume. (a) and (b) Snapshots from a deforming pillar captured at moments when the interface shows clear contrast. (c) Schematic illustration of dislocation configuration in the deformation volume.

ductile-type deformation is not abrupt: the engineering stress–strain curve at T_{set}=300 °C shows a short but obvious deviation from the linear segment right before the burst, indicating the occurrence of ductile-type process. Therefore, the critical transition temperature (T_c) is near 300 °C. To determine T_c with higher accuracy, another group of pillar samples was tested at set temperature between 250 °C and 375 °C (Fig. 8b), but with a smaller temperature interval of 25 °C. The T_c is well captured in this group of tests, i.e. ~275 °C ($T_{c,\ real}$=~240 °C), as indicated in the T_{set}=275 °C curve by the emergence of a series of small serrations above stress level of 600 MPa.

For stress–strain curves at set temperatures >275 °C, there are two characteristic stress values, i.e. a yield stress where the linear part ends, and a burst stress where the strain burst begins. The values of both stresses in Fig. 8a and b follow the same trend, i.e. monotonic decrease with increasing temperature. Since diffusive deformation is controlled by the driving force (stress in this work), diffusivity and diffusing time, the segment between the yield strength and the burst stress can best satisfy all three requirements, and therefore are the most diffusive-plasticity-dominated. For this reason, the continuous flow part will be referred to as diffusive plasticity hereafter. The diffusive plasticity can be corroborated by the change of sample shape right before the moment of strain burst, as shown in Fig. 8c–f. The diffusive plasticity results in a swollen part at the top of the pillar, indicating that the deformation volume is localized to just the top region. After unloading, no appreciable slip steps appear on the surfaces by SEM observation, indicating diffusive flow driven plasticity.

Based on the values of yield/burst stress at different temperatures, a two-dimensional DMM, similar to that of bulk materials, can be constructed using temperature as the abscissa and stress as the ordinate, as shown in Fig. 9. The estimated actual temperature is used according to Eq. (1), and is also plotted in terms of the homologous temperature ($T_h \equiv T/T_m$, where T is the absolute temperature and T_m is the absolute melting temperature). In DMM, there are three regimes each having a different dominant deformation mechanism, i.e. the elasticity, diffusive plasticity, and displacive plasticity. The lower line of the displacive plasticity regime is determined by values of burst stress at various temperatures, while the line between the elasticity regime and the diffusive plasticity regime by the values of yield stress at various temperatures. The stochastic-to-ductile transition temperature $T_{c,\ real}$=~240 °C is captured at the triple point of the two lines. The diffusive plasticity starts at the temperature higher than $T_{c,\ real}$ and dominates at medium stress levels between the elastic regime and the displacive plasticity regime. Such a DMM is useful for distinguishing among dominant deformation mechanisms and predicting the transition of deformation mode for a material subjected to any specific temperature-stress combination.

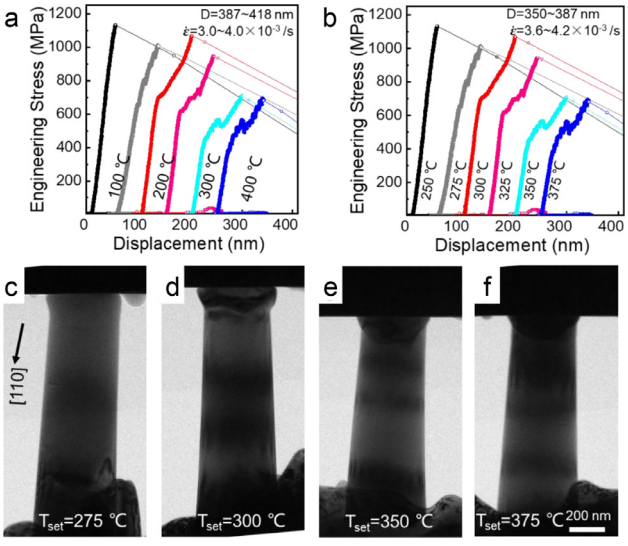

Fig. 8. The temperature dependence of deformation behavior for aluminum pillar with diameter of 350–420 nm at different set temperatures from 100 °C to 400 °C. (a) Eight engineering stress–displacement curves from the same group of aluminum pillars with diameter of 387–418 nm, tested at intervals of 100 °C, and two pillars were tested at each temperature. (b) Eight stress–displacement curves from another group of pillar samples, tested at temperature intervals of 25 °C from 250 °C to 375 °C. The diameter range is from 350 nm to 387 nm, slightly smaller than the group of (a). Curves in (a) and (b) are offset by 50 nm along the abscissa for clarity. (c–f) The TEM image of each pillar at the moment immediately before the burst at its corresponding testing temperature.

3.5. Sample size effect on mechanical behavior

The stochastic-to-ductile transition is not only present at a critical temperature T_c for a fixed sample size, but also at a critical size D_c at a given temperature. Fig. 10 shows the compression results of 12 pillar samples with diameters ranging from 118 nm to 985 nm, all at 275 °C and strain rates of 2.5–10.0 × $10^{-3}s^{-1}$. From the shape change in curves, D_c can be determined to be ~400 nm. Determination of the yield stress is unambiguous, but the starting stress for displacive plasticity is not, especially for curves without bursts. We choose the maximum flow stress before 10% plastic strain as the representative value. Finally, using pillar diameter (size) and stress as axes (Fig. 10b), another type of deformation mechanism map can be constructed, which also contains the same three regimes separated by the yield stress line and diffusive/displacive transition line. From Fig. 10b, the yield strength first increases with diameter and reaches a maximum value at D_c=~400 nm, then goes down at larger diameters. This reverted-U-shaped relationship is different from the monotonic relationship between yield strength and temperature. This result arises from the competition between diffusive plasticity and displacive plasticity. Below D_c, the yield strength shows a "smaller is much softer" trend [11] governed by diffusive plasticity. Since smaller samples have larger surface/volume ratio, shorter diffusion path, and higher stress-induced chemical potential gradient, the diffusive deformation starts at lower stress levels and its contribution becomes substantial quickly. Above D_c, the yield strength shows a classical "smaller is stronger" trend governed by displacive plasticity [1, 31].

The deformation at smaller size is more affected by the diffusive processes. A typical deformation process is shown in Fig. 11 with a pillar of D = 168 nm at T_{set}=275 °C and strain rate $\dot{\varepsilon}$=9.3 × 10^{-3}/s. After a short period of elastic deformation, the diffusive flow sets in at stress level of ~500 MPa, and continues all the way up to 1190 MPa. Like the previous example in Fig. 6, the true stress

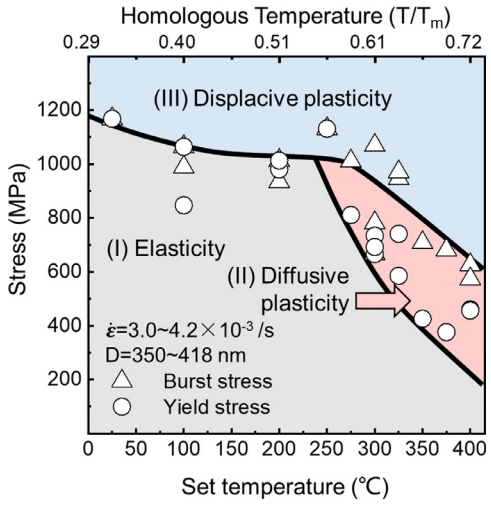

Fig. 9. The deformation mechanism map created based on the yield stresses and the burst stresses extracted from the stress–strain curves of (a) and (b) in Fig. 6. The size and strain rate ranges are indicated.

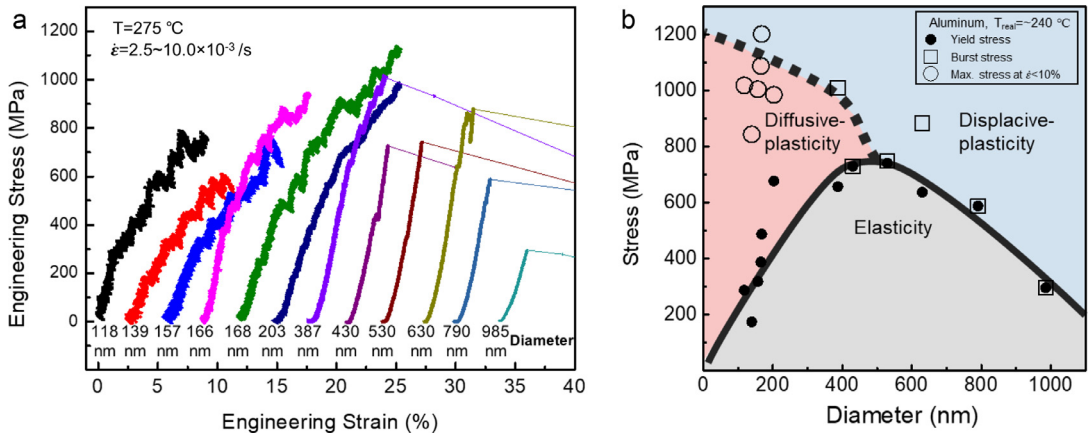

Fig. 10. The effect of pillar diameter on the deformation behavior at a fixed temperature of 275 °C. (a), Engineering stress–strain curves from a set of pillars with diameters ranging from 118 nm to 985 nm, tested at 275 °C and strain rates of 2.5–10.0 × 10^{-3} s^{-1}. Curves are offset by 2.5% along the abscissa for clarity (b) Deformation mechanism map has axes of pillar diameter and stress at the specific temperature of 275 °C. The black solid line and the black dashed line represent the yield stress and the maximum stress before burst or 10% plastic strain, respectively.

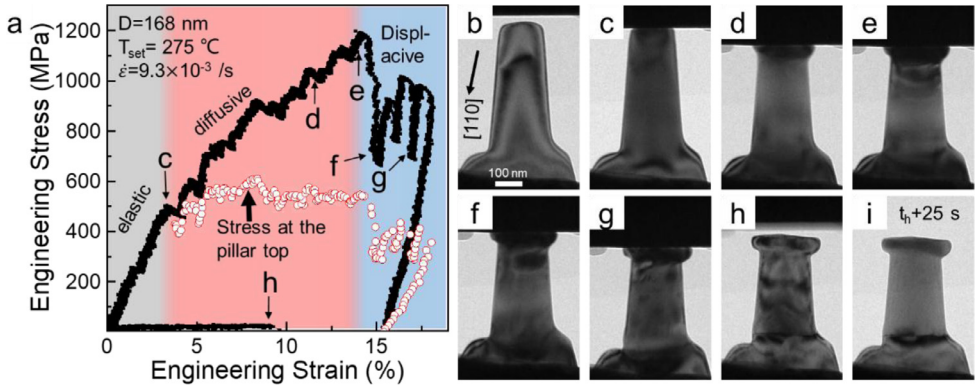

Fig. 11. Deformation process of a pillar of diameter D = 168 nm at T = 275 °C and strain rate $\dot{\varepsilon}$=9.3 × 10^{-3}/s. (a) The engineering stress–strain curve, which shows three distinct deformation stages, i.e. the elastic stage, the diffusive plastic stage, and the displacive plastic stage. The red circles represent the real stress at the top part of the pillar. (b) The bright field image of the well-annealed pillar before compression test. The compression is performed near [110] direction, as indicated with the black arrow. (c-h) The video snapshots showing the deformation process at moments indicated in (a). (i) Image of the pillar dynamically recovered for about 25 s at 275 °C after the compression test. (For interpretation of the references to color in this figure legend, the reader is referred to the web version of this article.)

calculated from dynamic change of diameter showed a plateau at the second stage, implying a steady-state balance of dislocation generation and escape/annihilation inside the deformation volume. In the following displacive part, the engineering stress–strain shows some small load drops at ~300 MPa and small strain bursts < 1%, in sharp contrast to the down-to-zero load drops and huge strain bursts of tens of percents in larger pillars. The dynamic evolution of morphology and internal defect configuration of the pillar is demonstrated with a few sequential images as shown in Fig. 11b–i (also in the supplementary movie s3). In the elasticity stage (Fig. 11b–c) and diffusive plasticity stage (Fig. 11d-e), the shape change and evolution of dislocation in the pillar are similar to those in Fig. 6. Localization of deformation in a small volume at the top of the pillar, together with a front interface impenetrable to incoming dislocations, is also evident (Fig. 11d and e). When a critical stress is approached (σ_c=~1190 MPa in this example), dislocations can break through the interface (Fig. 11e) and evolve in the whole pillar body, resulting in small strain bursts in the stress–strain curve as shown in Fig. 11f and g. In the supplementary movie s3, some of them rebound back from the bottom of the pillar as the stress decreases in the unloading part. The remaining dislocations are then thermally annealed out, leaving a low-angle grain boundary at the bottom part of the pillar, as can be seen at the moment immediately after retracting the diamond punch (Fig. 11h and supplementary movie s3). The quick change of dislocation configuration upon unloading indicates fast dynamic recovery under such an elevated testing temperature. After about 25 s, the dislocation in the pillar reached a steady state (Fig. 11i), with a clean interior except for the low angle grain boundary at the bottom part.

4. Summary

In summary, we systematically performed *in situ* quantitative mechanical tests on single crystal aluminum pillars of submicron diameters, under different temperatures covering the transition from fully dislocation-glide-based displacive plasticity to diffusive plasticity governed by power-law creep and/or diffusional creep. Based on these experimental data, we construct two styles of deformation mechanism maps, with stress-temperature and stress-sample-size coordinate system, respectively. These DMMs can be used to identify dominant deformation mechanisms, the critical condition for good formability, and the strongest size at particular temperature and strain rate.

Some interesting findings are:

1) Below T_c, the annealed submicron-pillars display a “stochastic” behavior. The stress–strain curve linearly climbs to a high stress point over 1 GPa, and then a giant strain burst occurs abruptly, with low controllability [9]. Above T_c, there is a continuous diffusive segment between the linear part and the strain burst, which

can be exploited to controllably shape crystals at size scale of a few hundreds of nanometers.

2) Transitions of deformation mechanism are surprisingly sharp, as observed not only in the deformation movies, but also in the stress–strain curves, when the temperature or stress goes across a critical value (T_c or σ_c). Both displacive and diffusive plasticity are found to be localized in the sample, but in different manners. Below T_c, it is strain burst along slip plane direction, while above T_c, it is continuous mushrooming at the top part of the pillars.
3) At a fixed temperature and strain rate, competition between the displacive deformation and the diffusive deformation will result in a “strongest sample size” where maximum yield strength is achieved. Below this critical size, the sample shows "smaller is weaker" behavior [11]. Above this critical size, the sample shows "smaller is stronger" behavior [24].
4) At temperature $T>T_c$, the diffusive plastic deformation is localized into a mushroom-shaped volume at the top part of the pillar. The smaller deformation volume compared to the displacive deformation probably arise from promoted cross-slip and climb of dislocations and pipe diffusion. Moreover, the deforming volume is demarcated by a moving front interface, which is likely a newly formed grain boundary. Dislocations coming from the deforming volume cannot penetrate this interface, but can only be absorbed into or follow behind it, until a critical high stress of ~1 GPa is reached.

Declaration of Competing Interest

The authors declare no competing financial interests.

CRediT authorship contribution statement

De-Gang Xie: Data curation and Formal analysis, Funding acquisition, Investigation and Methodology, Project administration, Writing - review & editing, Writing - original draft. **Rong-Rong Zhang:** Data curation and Formal analysis, Investigation and Methodology. **Zhi-Yu Nie:** Data curation and Formal analysis, Software. **Jing Li:** Conceptualization, Data curation and Formal analysis, Writing - original draft. **Evan Ma:** Writing - review & editing. **Ju Li:** Conceptualization, Writing - review & editing. **Zhi-Wei Shan:** Conceptualization, Funding acquisition, Project administration, Writing - review & editing.

Acknowledgments

The authors would like to thank Prof. Shigenobu Ogata (Osaka University) for the suggestion on FEM modeling, Yuanbin Qing and Qinqin Fu (Xi'an Jiaotong University) for the support on experimental tests. Moreover, the authors acknowledge funding from the National Key Research and Development Program of China (2017YFB0702001), Natural Science Foundation of China (51971169, 51701151), Shaanxi Postdoctoral Science Foundation (2017JQ5110), and the Natural Science Foundation of Shaanxi Province (2017JQ5110). J.L. acknowledges support by NSF DMR-1410636. E.M. acknowledges support from U.S. DoE-BES-DMSE, under Contract No. DE-FG02-16ER46056.

Supplementary materials

Supplementary material associated with this article can be found in the online version at doi:10.1016/j.actamat.2020.02.013.

References

[1] W.-Z. Han, L. Huang, S. Ogata, H. Kimizuka, Z.-C. Yang, C. Weinberger, Q.-J. Li, B.-Y. Liu, X.-X. Zhang, J. Li, E. Ma, Z.-W. Shan, From “smaller is stronger” to “size-independent strength plateau”: towards measuring the ideal strength of iron, Adv. Mater. 27 (2015) 3385–3390.
[2] L.Y. Chen, M.R. He, J. Shin, G. Richter, D.S. Gianola, Measuring surface dislocation nucleation in defect-scarce nanostructures, Nat. Mater. 14 (2015) 707–713.
[3] Z.W. Shan, R.K. Mishra, S.A.S. Asif, O.L. Warren, A.M. Minor, Mechanical annealing and source-limited deformation in submicrometre-diameter Ni crystals, Nat. Mater. 7 (2008) 115–119.
[4] Z.-J. Wang, Q.-J. Li, Y.-N. Cui, Z.-L. Liu, E. Ma, J. Li, J. Sun, Z. Zhuang, M. Dao, Z.-W. Shan, Cyclic deformation leads to defect healing and strengthening of small-volume metal crystals, Proc. Natl. Acad. Sci. 112 (2015) 13502–13507.
[5] M.B. Lowry, D. Kiener, M.M. LeBlanc, C. Chisholm, J.N. Florando, J.W. Morris, A.M. Minor, Achieving the ideal strength in annealed molybdenum nanopillars, Acta Mater. 58 (2010) 5160–5167.
[6] Z.-J. Wang, Z.-W. Shan, J. Li, J. Sun, E. Ma, Pristine-to-pristine regime of plastic deformation in submicron-sized single crystal gold particles, Acta Mater. 60 (2012) 1368–1377.
[7] F.F. Csikor, C. Motz, D. Weygand, M. Zaiser, S. Zapperi, Dislocation avalanches, strain bursts, and the problem of plastic forming at the micrometer scale, Science 318 (2007) 251–254.
[8] D.M. Dimiduk, C. Woodward, R. LeSar, M.D. Uchic, Scale-free intermittent flow in crystal plasticity, Science 312 (2006) 1188–1190.
[9] Z. Wang, Z. Shan, J. Li, J. Sun, E. Ma, An index for deformation controllability of small-volume materials, Sci. China Technol. Sci. 57 (2014) 663–670.
[10] J. Sun, L.B. He, Y.C. Lo, T. Xu, H.C. Bi, L.T. Sun, Z. Zhang, S.X. Mao, J. Li, Liquid-like pseudoelasticity of sub-10-nm crystalline silver particles, Nat. Mater. 13 (2014) 1007–1012.
[11] L. Tian, J. Li, J. Sun, E. Ma, Z.W. Shan, Visualizing size-dependent deformation mechanism transition in Sn, Sci. Rep. 3 (2013) 2113.
[12] W. Guo, Z. Wang, J. Li, Diffusive versus displacive contact plasticity of nanoscale asperities: temperature- and velocity-dependent strongest size, Nano Lett. 15 (2015) 6582–6585.
[13] D. Xie, Z. Wang, J. Sun, J. Li, E. Ma, Z. Shan, In situ study of the initiation of hydrogen bubbles at the aluminium metal/oxide interface, Nat. Mater. 14 (2015) 899–903.
[14] L. Zhong, F. Sansoz, Y. He, C. Wang, Z. Zhang, S.X. Mao, Slip-activated surface creep with room-temperature super-elongation in metallic nanocrystals, Nat. Mater. 16 (2017) 439–445.
[15] L.M. Brown, Power laws in dislocation plasticity, Philos. Mag. 96 (2016) 2696–2713.
[16] A.B. Pandey, R.S. Mishra, A.G. Paradkar, Y.R. Mahajan, Steady state creep behaviour of an Al-Al_2O_3 alloy, Acta Mater. 45 (1997) 1297–1306.
[17] X. Huang, N. Hansen, N. Tsuji, Hardening by annealing and softening by deformation in nanostructured metals, Science 312 (2006) 249.
[18] F.G. Sen, A.T. Alpas, A.C.T. van Duin, Y. Qi, Oxidation-assisted ductility of aluminium nanowires, Nat. Commun. 5 (2014) 3959.
[19] Y. Yang, A. Kushima, W. Han, H. Xin, J. Li, Liquid-like, self-healing aluminum oxide during deformation at room temperature, Nano Lett. 18 (2018) 2492–2497.
[20] M.F. Ashby, A first report on deformation-mechanism maps, Acta Metall. 20 (1972) 887–897.
[21] V. Yamakov, D. Wolf, S.R. Phillpot, A.K. Mukherjee, H. Gleiter, Deformation-mechanism map for nanocrystalline metals by molecular-dynamics simulation, Nat. Mater. 3 (2004) 43–47.
[22] S.M. Keralavarma, A.A. Benzerga, High-temperature discrete dislocation plasticity, J. Mech. Phys. Solids 82 (2015) 1–22.
[23] H. Lüthy, R.A. White, O.D. Sherby, Grain boundary sliding and deformation mechanism maps, Mater. Sci. Eng. 39 (1979) 211–216.
[24] T. Zhu, J. Li, Ultra-strength materials, Prog. Mater. Sci. 55 (2010) 710–757.
[25] S. Suresh, J. Li, Deformation of the ultra-strong, Nature 456 (2008) 716–717.
[26] T. Zhu, J. Li, A. Samanta, A. Leach, K. Gall, Temperature and strain-rate dependence of surface dislocation nucleation, Phys. Rev. Lett. 100 (2008) 025502.
[27] C. Ayas, J.A.W. van Dommelen, V.S. Deshpande, Climb-enabled discrete dislocation plasticity, J. Mech. Phys. Solids 62 (2014) 113–136.
[28] S.P. Baker, Y.C. Joo, M.P. Knauss, E. Arzt, Electromigration damage in mechanically deformed Al onductor lines: dislocations as fast diffusion paths, Acta Mater. 48 (2000) 2199–2208.
[29] S.G. Srinivasan, X.Z. Liao, M.I. Baskes, R.J. McCabe, Y.H. Zhao, Y.T. Zhu, Compact and dissociated dislocations in aluminum: implications for deformation, Phys. Rev. Lett. 94 (2005) 125502.
[30] M. Legros, G. Dehm, E. Arzt, T.J. Balk, Observation of giant diffusivity along dislocation cores, Science 319 (2008) 1646–1649.
[31] M.D. Uchic, P.A. Shade, D.M. Dimiduk, Plasticity of micrometer-scale single crystals in compression, Annu. Rev. Mater. Res. 39 (2009) 361–386.
[32] Q. Yu, M. Legros, A.M. Minor, In situ tem nanomechanics, MRS Bull. 40 (2015) 62–70.
[33] M.E. DeCoster, K.E. Meyer, B.D. Piercy, J.T. Gaskins, B.F. Donovan, A. Giri, N.A. Strnad, D.M. Potrepka, A.A. Wilson, M.D. Losego, P.E. Hopkins, Density and size effects on the thermal conductivity of atomic layer deposited TiO_2 and Al_2O_3 thin films, Thin Solid Films 650 (2018) 71–77.
[34] S. Lee, J. Jeong, Y. Kim, S.M. Han, D. Kiener, S.H. Oh, FIB-induced dislocations in Al submicron pillars: annihilation by thermal annealing and effects on deformation behavior, Acta Mater. 110 (2016) 283–294.
[35] D. Kiener, Z. Zhang, S. Šturm, S. Cazottes, P.J. Imrich, C. Kirchlechner, G. Dehm, Advanced nanomechanics in the TEM: effects of thermal annealing on FiB prepared Cu samples, Philos. Mag. 92 (2012) 3269–3289.
[36] J.M. Wheeler, C. Kirchlechner, J.-S. Micha, J. Michler, D. Kiener, The effect of size on the strength of fcc metals at elevated temperatures: annealed copper, Philos. Mag. 96 (2016) 3379–3395.
[37] R.C. Picu, D. Zhang, Atomistic study of pipe diffusion in Al-Mg alloys, Acta Mater. 52 (2004) 161–171.

[38] R.W. Balluffi, R.M. Thomson, Kinetic theory of dislocation climb. 2. Steady state edge dislocation climb, J. Appl. Phys. 33 (1962) 817.
[39] V.K. Lindroos, H.M. Miekk-oja, Knitting of dislocation networks by means of stress-induced climb in an aluminium-magnesium alloy, Philos. Mag.: J. Theor. Exp. Appl. Phys. 17 (1968) 119–133.
[40] V.K. Lindroos, H.M. Miekk-Oja, The structure and formation of dislocation networks in aluminium-magnesium alloys, Philos. Mag.: J. Theor. Exp. Appl. Phys. 16 (1967) 593–610.
[41] G.M. Bond, I.M. Robertson, F.M. Zeides, H.K. Birnbaum, Subthreshold electron irradiation damage in hydrogen-charged aluminum, Philos. Mag. A – Phys. Condens. Matter Struct. Defects Mech. Prop. 55 (1987) 669–681.
[42] S.B. Fisher, On the temperature rise in electron irradiated foils, Radiat. EIT 5 (1970) 239–243.
[43] M. Watanabe, T. Someya, Y. Nagahama, Temperature rise of specimen due to electron irradiation, J. Phys. D: Appl. Phys. 3 (1970) 1461.
[44] S. Kritzinger, E. Ronander, Local beam heating in metallic electron-microscope specimens, J. Microsc. 102 (1974) 117–124.
[45] Y. Cui, G. Po, N. Ghoniem, Does irradiation enhance or inhibit strain bursts at the submicron scale? Acta Mater. 132 (2017) 285–297.
[46] M. Victoria, N. Baluc, C. Bailat, Y. Dai, M.I. Luppo, R. Schäublin, B.N. Singh, The microstructure and associated tensile properties of irradiated fcc and bcc metals, J. Nucl. Mater. 276 (2000) 114–122.
[47] J. Silcox, M. Whelan, Direct observations of the annealing of prismatic dislocation loops and of climb of dislocations in quenched aluminium, Philos. Mag. 5 (1960) 1–23.